Caliphate Journal of Science & Technology (CaJoST)

ISSN: 2705-313X (PRINT); 2705-3121 (ONLINE) Research Article

Open Access Journal available at: https://cajost.com.ng/index.php/files and https://www.ajol.info/index.php/cajost/index

DOI: https://dx.doi.org/10.4314/cajost.v6i2.13

Article Info

Received: 20th April 2024

Revised: 25th July 2024

Accepted: 26th July 2024

Department of Physics, Sokoto State University, Sokoto Nigeria

***Corresponding author's email:**

usman.iliyasu@ssu.edu.ng

Cite this: *CaJoST*, 2024, 2, 236-248

Photon and Neutron Characterization of Titanium Neodymium Tellurite Glass Doped WO_3

Usman Iliyasu and Anas Shehu

This study investigates the photon and neutron attenuation properties of a glass system comprising [(89-x)TeO_2+10TiO_2+1Nd_2O_3+xWO_3], where x=0, 10, and 20 mol%. Utilizing Phy-X and XCOM programs, the mass attenuation coefficient was determined in the energy range 0.015 to 15 MeV. The results show that the mass attenuation coefficient at 0.015 MeV increased by 6.66% and 12.74% with the addition of 10 mol% and 20 mol% WO_3, respectively. Similarly, The HVL of the glass samples decreased by 6% and 16% with the addition of 10 mol% and 20 mol% WO_3, respectively. The exposure buildup factor and energy absorption buildup factor decreased with increasing WO_3 content and increased with penetration depth. Notably, the fast neutron removal cross-section of TW20 surpasses that of some standard shielding materials. These findings suggest that the TW20 glass sample, with highest WO_3 content, exhibits promising gamma and neutron shielding applications.

Keywords: Tellurite glass; Phy-X; Tungsten oxide; Mass attenuation coefficient; Mean free path.

1. Introduction

Advances in understanding ionizing radiation and neutrons have led to various medical applications, including diagnostic imaging (X-rays, CT scans), sterilization of medical instruments, and industrial uses like inspecting metals and analyzing materials. Research reactors utilize neutron activation analysis and produce radioisotopes, while agricultural applications include investigating soil parameters and calculating crop nutrition and water requirements. However, despite the benefits, ionizing radiation poses significant risks, including genetic mutations, cancer, skin burns, radiation sickness, and other harmful health effects, highlighting the need for careful management and safety measures. The search for a reliable material to protect humans and the environment from harmful radiation is crucial. Radiation shielding materials aim to reduce or block photons and neutrons to a safe level. Researchers have explored various materials, including regular concrete and concrete reinforced with different additives, to find the most effective solution for radiation protection [1, 2] concrete doped nanoparticles [3-5], Polymers [6]in an effort to identify optimal materials for this critical application. While concrete, alloys, and polymers have potential as radiation shielding materials, they also have significant limitations. Concrete, in particular, has several drawbacks, including: Lack of transparency, making it difficult to monitor the protected area, requires large space, and Prone to cracking and damage from humidity, which affects its performance and reliability [7]; alloys, on the other hand, are prone to corrosion when exposed to the damp environment [8, 9].

Glass materials have proven to be a promising solution for shielding both ionizing and non-ionizing radiation, especially when modified with heavy metal oxides and transition metals. The addition of these elements significantly enhances the glass's ability to absorb radiation, making it a highly effective material for radiation shielding purposes [10, 11]. Furthermore, the transparency of this glass enables clear visualization of the internal environment, making it an ideal material for applications such as X-ray rooms, where visibility is crucial. This glass allows for unobstructed viewing, even in areas where radiation shielding is necessary, ensuring both safety and visibility. [12, 13]. The versatility of glass as a material lies in its ability to be tailored with a wide range of chemical components, enabling the enhancement of its physical and chemical properties. By incorporating heavy metals or transition metals, such as Bi_2O_3, PbO, and WO_3, the properties of glass can be modified to suit specific applications, making it a highly adaptable and valuable material for various uses [14, 15].

Unlike other oxide glass formers, TeO_2 has a unique characteristic: it can only form glass when combined with heavy metal oxides or transition metal oxides. Moreover, its ability to reduce the glass transition temperature, as reported by Yasser et al. [16] makes it a superior choice for glass formation, offering improved properties and versatility in glass design. Additionally, its stability and non-toxicity make it a highly versatile material, suitable for a wide range of applications. Some of the areas where it shows great promise include energy storage, optoelectronics, medicine, electronic materials, and catalysis. Its unique combination of properties makes it an attractive material for various industries, enabling innovative solutions and technologies [15, 17].

Numerous studies have confirmed that TeO_2 -based glasses exhibit improved photon attenuation, which increases significantly with higher TeO_2 content. The high density of TeO_2 is responsible for this enhancement, allowing the material to effectively absorb radiation and improve the shielding properties of the glass. Research by Aloraini et al. [18] provides a notable example, demonstrating the significant enhancement in photon attenuation that occurs when TeO_2 is added to strontium borate tellurite glasses, further highlighting the potential of TeO_2 for radiation shielding applications. Studies have shown that tellurite glasses containing MgO, as reported by Hanfi et al. [19], possess outstanding optical and photon attenuation properties. Moreover, Alalawi et al. discovered that a glass composite comprising TeO2, PbO, and zinc exhibits excellent radiation shielding properties. Several other investigations have also explored the radiation shielding capabilities of TeO_2, further solidifying its reputation as a promising material for this application. Neodymium oxide (Nd_2O_3), a rare earth oxide, has been widely used as a glass additive to improve optical properties, structural stability, and radiation shielding capabilities [20], [21]. Numerous studies have consistently demonstrated that the incorporation of Nd_2O_3 into a glass matrix results in a significant increase in glass density [21-23]. Additionally, Nd_2O_3 has proven valuable in specialized applications, including laser technology and optical limiting devices, where its unique properties enable advanced functionality [24]. Research has shown that the incorporation of WO_3 into a glass matrix leads to an increase in band gap energy and a decrease in the glass refractive index [37]. Studies conducted by Iliyasu et al. [25], Al-buriahi et al. [26], and Alzahrani et al. [27] have consistently demonstrated that the optical and radiation shielding capabilities of glass are significantly enhanced through the addition of WO_3, making it a valuable component in the design of radiation shielding materials.

This research investigates the effects of different WO_3 concentrations on the $(89\text{-}x)TeO_2–10TiO_2–1Nd_2O_3–xWO_3$ glass system, with a focus on photon and neutron shielding properties using the Phy-X software. Simulation programs like Phy-X have been rigorously tested and validated, showing excellent agreement with experimental results, with a deviation of less than 5%. For example, Aloraini et al. [28] and Abouhaswa et al. [29] demonstrated the accuracy of Phy-X/PSD in predicting the radiation shielding properties of various glass materials, with a discrepancy of less than 5% compared to experimental values. These findings highlight the reliability of simulation software in materials science research. Furthermore, Mhareb et al. [30] investigated the radiation protection properties of zinc sodium barium borate glasses by experimental and XCOM programs, and the deviation was less than 4%.The mass attenuation coefficient was simulated from which the effective atomic number, mean free path, energy buildup factor EBF, and energy absorption buildup factor EABF were calculated. The mass attenuation coefficients were verified by comparison with XCOM data. Additionally, the glass system's neutron shielding properties were evaluated, and its fast neutron removal cross-sections were compared to those of other standard shielding materials, providing valuable insights into its photon and neutron shielding performance.

2. Materials and Methods

The glass series of the form $(89\text{-}x)TeO_2–10TiO_2–1Nd_2O_3–xWO_3$, where x=0, 10, and 20 mol% have been synthesized using the melt-quench techniques. The TeO_2, TiO_2, Nd_2O_3, and WO_3 were of standard grade 99.9% (Sigma Alderich). The material was pulverized in a mortar with a pestle for 1 hour, then heated in an electric furnace at 900°C using a platinum crucible for 1 hour. Next, the molten material was promptly transferred to a second furnace at 300°C for annealing, a process that relieves thermal shock and fatigue by allowing the material to slowly cool and relax. Further information on the synthesis, structural properties, and optical properties of the glasses can be found in the work by Kebaili et al. [31]. A comprehensive description of the composition and density of the glasses is given in Table 1. For this study, the glasses are coded TW0, TW10, and TW20 for $89TeO_2+10TiO_2+1Nd_2O_3$, $79TeO_2+10TiO_2+1Nd_2O_3+10WO_3$, and $69TeO_2+10TiO_2+1Nd_2O_3+20WO_3$ samples, respectively.

Table 1. Composition and densities of the investigated glass samples

	Mole fraction of compounds (mol%)				Mole fraction of elements (mol%)					
Glass samples	**TeO_2**	**TiO_2**	**Nd_2O_3**	**WO_3**	**Te**	**O**	**Ti**	**Nd**	**W**	**Density g/cm^3**
WT0	89.000	10.000	1.000	0.000	0.2947	0.6656	0.0331	0.0066	0.0000	5.2310
WT10	79.000	10.000	1.000	10.000	0.2532	0.6763	0.0321	0.0064	0.0321	5.5790
WT20	69.000	10.000	1.000	20.000	0.2143	0.6863	0.0311	0.0062	0.0621	5.9440

Phy-X and XCOM online simulation code were used to calculate the shielding parameters of the investigated glasses. Phy-X and XCOM software is straightforward to use, has easy accessibility, and has a user-friendly interface available at https://phy-x.net/PSD [32] and XCOM online program [33]. The Phy-X program required one to register, followed by defining the chemical composition and density of the materials. The other part required the selection of energy range and parameters to be evaluated.

2.2.2. Mass attenuation coefficient MAC

MAC is a parameter that quantifies the fraction of photons attenuated when they pass through a material absorber per unit mass [34].

$$\mu_m = {}^{\mu}/_{\rho} = \sum_i w_i ({}^{\mu}/_{\rho})_i \quad (1)$$

ρ is the absorber's density (g/cm^3), and w_i is the weight fraction of the ith compound absorber.

μ_m is a critical quantity in radiation design because it quantifies the total interaction cross-section contributed by all of the key partial interaction modes. Photoelectric interaction Pe, Compton scattering Cs, and pair production Pp effect make up the main interaction mode.

For photon energies under 20 MeV, the total, partial interaction cross-section is given by the equation [35]:

$$\sigma_T = \sigma_{\mathrm{Pe}} + \sigma_{\mathrm{Cs}} + \sigma_{\mathrm{Pp}} \quad (2)$$

where σ_T represents the total cross-section resulting from the partial photoelectric, Compton scattering, and pair annihilation cross-section.

The following equation represents the mass attenuation coefficient in terms of the total partial cross-sections [36]:

$$\mu_m = \frac{N_A}{W}\sigma_T = \frac{N_A}{W}\left(\sigma_{\mathrm{Pe}} + \sigma_{\mathrm{Cs}} + \sigma_{\mathrm{Pp}}\right) = \mu_{\mathrm{Pe}} + \mu_{\mathrm{Cs}} + \mu_{\mathrm{Pp}} \quad (3)$$

W represents the atomic weight of the absorber, N_A is a constant called Avogadro's number.

Therefore,

The combined mass attenuation coefficients given by the three interaction modes are shown in the following equation [35]:

$$\mu_m = \mu_{\mathrm{Pe}} + \mu_{\mathrm{Cs}} + \mu_{\mathrm{Pp}} \quad (4)$$

2.2.3. Half value layer HVL

HVL represents the thickness (cm) of an absorber that is needed to reduce the energy of incident photons by 1/2. The HVT of the glass can be calculated using the expression in the following equation [37]:

$$HVT = {}^{Ln2}/_{\mu} \quad (5)$$

HVT is influenced by the density of the interacting medium and the photon energy of the absorber.

2.2.4. Mean free path MFP

The average distance photons travel in an absorber material prior to a successful interaction is known as the mean free path [35].

$$MFP = {}^{1}/_{\mu} \quad (6)$$

MFP is also influenced by the density of the interacting medium and photon energy.

2.2.6 G-P fittings parameter

The calculated $Z_{eq}$of TW0, TW10, and TW20 glasses have been used to calculate the G-P fittings parameters $(b, c. a, X_k, and\ d)$ using the expression [38]:

$$P = \frac{P_1(logZ_2 - logZ_{eq}) + P_2(log\ Z_{eq} - logZ_1)}{logZ_2 - logZ_1} \quad (7)$$

P_1 and P_2 represent the G-P fitting parameters corresponding to the atomic numbers Z_1 and Z_2, respectively.

2.2.7. Photons Buildup factor

G-P fittings parameters were deployed to calculate the EBF and EABF of TW0, TW10, and TW20 glasses using the following expression [39]:

$$B(E, X) = 1 + \frac{b-1}{k-1}(K^x - 1) \text{ for } k \neq 1 \quad (8)$$

$$B(E,X) = 1 + (b-1)x \text{ for } k = 1, \quad (9)$$

where

$$K(E,X) = cx^a + d\frac{\tanh\left(\frac{x}{X_k}-2\right)-\tanh(-2)}{1-\tanh(-2)} \text{ for } x \leq 40, \quad (10)$$

Where E represents the photon's energy, x represents the penetration depth in mfp, and $(K(E,X))$ represents the dose multiplicative factor.

2.2.11. Relative deviation

The relative deviation for Phy-X/PSD and XCOM software is calculated from the following equation:

$$R.Dev.(\%) = \frac{\left(\frac{\mu}{\rho}\right)_{Phy-X} - \left(\frac{\mu}{\rho}\right)_{XCOM}}{\left(\frac{\mu}{\rho}\right)_{Phy-X}} \times 100 \quad (11)$$

3. Results and Discussion

Being independent of absorber density, the mass attenuation coefficient is the most important factor when studying the shielding properties of a material. The total mass attenuation coefficient is the sum of all the contributions from photoelectric absorption, inelastic Compton scattering, and annihilation cross sections, as described in equation (4). The MAC of the (89-x)TeO_2–10TiO_2– 1Nd_2O_3–xWO_3 glasses obtained using Phy-X are compared with XCOM values within the photon energy range of 0.015 to 15 MeV. The results were quite consistent with a maximum difference of less than 1%. Based on the findings, it can be concluded that photon interactions with TW glasses are predominantly influenced by photoelectric interaction, inelastic Compton scattering, and pair annihilation modes. The largest MAC values occurred at lower photon energies due to photoelectric event dominance caused by photon absorption. While it diminishes as photon energy increases for all studied glasses due to Compton scattering and pair production.

At intermediate photon energies, inelastic Compton scattering dominated the interaction mode, and the MAC reduced significantly as photon energy increased. Furthermore, as the pair-producing mode dominates the interaction process, the MAC remains almost constant at increased photon energy. As shown in Fig. 1, the investigated TW0 glass has a MAC value of 40.586 cm^2/g at 0.015 MeV, and replacing part of the TeO_2 with 10 mol% and 20 mol% WO_3 results in an increased MAC by 6.66 % and 12.74 %, for TW10 and TW20 respectively. The elevated MAC values for the examined glasses are due to WO_3 density (7.16 g/cm^3) being greater than TeO_2 density (5.67 g/cm^3). MAC decreases with increasing photon energy until a sudden discontinuity is observed at 30 KeV and is attributed to K-absorption edges of (W) appearing in the area where the photoelectric effect is dominant. The point at which the K-absorption edge occurred corresponds to MAC values of 7.998 and 9.547 cm^2/g for the TW10 and TW20 glasses, respectively.

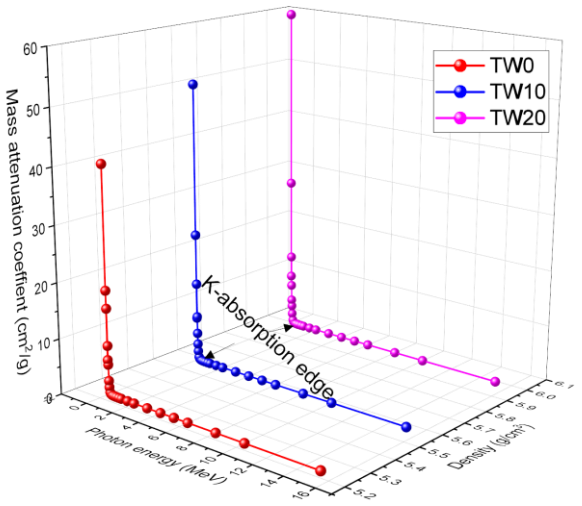

Figure 1. Mass attenuation coefficient of the WT glass sample as a function of photon energy and WO_3 concentrations.

Above 1 MeV, the MAC value steadily decreased as the photon energy increased to 4 MeV due to multiple photo scattering and the Compton scattering probability cross section depends linearly on (Z). Above 5 MeV, the probability of pair-production events dominates the interaction. The MAC value does not change significantly but remains nearly constant The MACs of the studied glasses drop to a minimum at 15 MeV, corresponding to 0.037, 0.039, and 0.040 for WT0, WT10, and WT20, respectively, as presented in Table 1. The study found that the glass sample encoded WT20 with the highest WO_3 content (20 mol%) had the highest MAC value, and WT0 (without WO_3) had the lowest MAC value.

Table 2. Mass attenuation coefficient (cm^2/g) of the TW0, TW10, and TW20 glasses

Photon energy			WT0			WT10			WT20
MeV	Phy-X	XCOM	Dev. %	Phy-X	XCOM	Dev. %	Phy-X	XCOM	Dev. %
0.015	40.586	40.590	0.010	50.641	50.610	0.061	59.831	59.800	0.053
0.02	18.701	18.700	0.005	23.531	23.520	0.046	27.945	27.930	0.053
0.03	6.302	6.302	0.006	7.998	7.993	0.057	9.547	9.543	0.047
0.04	15.518	15.520	0.015	14.403	14.400	0.023	13.385	13.380	0.036
0.05	8.869	8.870	0.006	8.244	8.244	0.002	7.673	7.670	0.034
0.06	5.470	5.471	0.013	5.092	5.091	0.016	4.746	4.744	0.040
0.08	2.549	2.549	0.017	3.071	3.069	0.060	3.548	3.546	0.060
0.1	1.425	1.425	0.012	1.727	1.726	0.061	2.003	2.002	0.064
0.15	0.532	0.532	0.006	0.639	0.639	0.058	0.737	0.736	0.051
0.2	0.293	0.293	0.006	0.344	0.343	0.054	0.390	0.390	0.034
0.3	0.154	0.154	0.026	0.172	0.172	0.014	0.188	0.188	0.026
0.4	0.112	0.112	0.028	0.120	0.120	0.010	0.128	0.128	0.044
0.5	0.092	0.095	3.316	0.097	0.097	0.018	0.102	0.102	0.006
0.6	0.080	0.080	0.002	0.084	0.084	0.007	0.087	0.087	0.007
0.8	0.067	0.067	0.004	0.068	0.068	0.001	0.070	0.070	0.008
1	0.058	0.058	0.002	0.059	0.059	0.003	0.060	0.060	0.003
1.5	0.047	0.047	0.005	0.047	0.047	0.008	0.048	0.048	0.006
2	0.041	0.041	0.004	0.042	0.042	0.004	0.042	0.042	0.009
3	0.036	0.036	0.009	0.037	0.037	0.007	0.037	0.037	0.007
4	0.034	0.034	0.001	0.035	0.035	0.006	0.035	0.035	0.000
5	0.033	0.033	0.007	0.034	0.034	0.004	0.035	0.035	0.002
6	0.033	0.033	0.007	0.034	0.034	0.010	0.035	0.035	0.006
8	0.034	0.034	0.006	0.035	0.035	0.010	0.035	0.035	0.002
10	0.035	0.035	0.001	0.036	0.036	0.021	0.037	0.037	0.020
15	0.037	0.037	0.014	0.039	0.039	0.029	0.040	0.040	0.023

Table 3. G-P fitting parameters for EBF and EABF of TW0 glass.

G-P Fitting Parameters for EBF					*G-P Fitting Parameters for EABF*				
a	**b**	**c**	**d**	**Xk**	**a**	**b**	**c**	**d**	**Xk**
-0.397	1.005	1.298	0.292	5.989	-0.394	1.005	1.295	0.287	6.722
0.509	1.013	0.209	-0.482	11.263	0.301	1.012	0.286	-0.265	16.458
0.198	1.034	0.374	-0.275	25.541	0.249	1.033	0.328	-0.182	17.584
0.091	3.808	0.647	-0.066	24.436	0.100	1.551	0.660	-0.038	19.642
-0.033	3.289	0.253	-0.083	14.260	0.052	1.505	0.261	-0.049	12.283
0.522	2.684	0.122	-0.101	11.094	0.349	1.451	0.143	-0.065	18.123
0.792	1.744	0.024	-0.198	14.991	0.663	1.352	0.055	-0.228	14.153
0.526	1.299	0.155	-0.254	13.774	0.524	1.279	0.144	-0.281	13.565
0.241	1.227	0.385	-0.132	14.120	0.377	1.441	0.232	-0.208	13.947

0.172	1.333	0.505	-0.094	14.508	0.323	1.846	0.291	-0.194	13.957
0.098	1.462	0.674	-0.048	14.311	0.191	2.063	0.488	-0.111	13.894
0.057	1.584	0.819	-0.040	14.152	0.138	2.384	0.627	-0.102	13.882
0.035	1.657	0.902	-0.032	14.138	0.096	2.459	0.742	-0.079	13.879
0.018	1.687	0.960	-0.023	13.998	0.072	2.468	0.808	-0.066	13.738
0.004	1.716	1.019	-0.017	14.071	0.045	2.391	0.893	-0.051	13.638
-0.003	1.712	1.046	-0.015	13.430	0.031	2.289	0.938	-0.042	13.514
-0.024	1.590	1.136	-0.003	11.673	-0.001	1.926	1.056	-0.021	13.590
-0.019	1.584	1.120	-0.007	12.804	0.009	1.850	1.027	-0.030	13.089
0.000	1.555	1.065	-0.029	12.847	0.035	1.720	0.955	-0.058	13.213
0.016	1.507	1.023	-0.042	13.341	0.052	1.597	0.911	-0.073	13.545
0.044	1.516	0.947	-0.067	13.564	0.079	1.560	0.846	-0.097	13.810
0.053	1.490	0.929	-0.075	13.759	0.088	1.500	0.829	-0.105	14.031
0.074	1.507	0.889	-0.093	14.063	0.101	1.454	0.814	-0.115	14.258
0.056	1.470	0.965	-0.075	14.165	0.080	1.385	0.890	-0.094	14.347
0.038	1.513	1.095	-0.061	14.210	0.062	1.364	1.006	-0.081	14.364

Table 4. G-P fitting parameters for EBF and EABF of TW10 glass.

G-P Fitting Parameters for EBF					*G-P Fitting Parameters for EABF*				
a	**b**	**c**	**d**	**Xk**	**a**	**b**	**c**	**d**	**Xk**
-0.533	1.004	1.603	0.344	6.078	-0.533	1.004	1.603	0.344	6.078
0.641	1.012	0.126	-0.682	11.300	0.337	1.009	0.254	-0.327	17.396
0.194	1.026	0.370	-0.248	24.835	0.251	1.024	0.332	-0.188	16.900
0.090	3.861	0.517	-0.052	24.009	0.103	1.526	0.524	-0.041	21.074
-0.118	3.235	0.189	-0.042	13.576	-0.009	1.468	0.199	0.002	11.097
0.682	2.608	0.090	-0.114	12.854	0.472	1.417	0.110	-0.100	17.243
0.809	1.801	0.018	-0.157	15.402	0.726	1.389	0.036	-0.227	14.231
0.688	1.396	0.056	-0.322	13.792	0.659	1.337	0.069	-0.359	13.412
0.287	1.217	0.318	-0.160	13.931	0.439	1.437	0.174	-0.240	13.850
0.174	1.251	0.493	-0.094	14.560	0.336	1.609	0.273	-0.196	13.909
0.111	1.385	0.633	-0.053	14.151	0.218	1.895	0.434	-0.124	13.763
0.070	1.504	0.770	-0.044	14.135	0.163	2.217	0.566	-0.114	13.868
0.047	1.578	0.853	-0.037	14.070	0.115	2.296	0.683	-0.089	13.873
0.029	1.614	0.916	-0.026	13.962	0.090	2.338	0.751	-0.075	13.724
0.012	1.655	0.980	-0.020	13.964	0.060	2.308	0.842	-0.058	13.624
0.005	1.660	1.013	-0.018	13.374	0.044	2.233	0.892	-0.049	13.509
-0.019	1.564	1.113	-0.006	14.186	0.010	1.933	1.016	-0.028	13.639
-0.017	1.562	1.111	-0.008	13.035	0.017	1.849	1.000	-0.037	13.113
0.002	1.542	1.062	-0.030	12.908	0.040	1.717	0.941	-0.063	13.237
0.016	1.496	1.026	-0.043	13.379	0.056	1.596	0.902	-0.078	13.552
0.046	1.514	0.945	-0.071	13.607	0.085	1.568	0.832	-0.104	13.798

0.057	1.495	0.922	-0.080	13.831	0.097	1.514	0.809	-0.115	14.011
0.080	1.531	0.879	-0.098	14.150	0.111	1.480	0.792	-0.125	14.291
0.059	1.500	0.965	-0.078	14.207	0.087	1.411	0.879	-0.101	14.350
0.035	1.565	1.115	-0.060	14.167	0.063	1.401	1.016	-0.084	14.291

Table 5. G-P fitting parameters for EBF and EABF of TW20 glass.

G-P Fitting Parameters for EBF					*G-P Fitting Parameters for EABF*				
a	**b**	**c**	**d**	**Xk**	**a**	**b**	**c**	**d**	**Xk**
-0.396	1.002	1.875	0.287	9.204	-0.396	1.002	1.875	0.287	9.204
0.723	1.010	0.111	-0.934	10.954	0.407	1.007	0.238	-0.448	14.215
0.203	1.021	0.361	-0.094	14.788	0.248	1.019	0.362	-0.179	12.485
0.089	3.914	0.388	-0.039	23.587	0.106	1.502	0.389	-0.043	22.491
-0.203	3.181	0.125	0.000	12.888	-0.071	1.432	0.136	0.053	9.907
0.840	2.533	0.057	-0.126	14.609	0.595	1.383	0.077	-0.134	16.365
0.485	1.892	0.085	-0.076	15.775	0.458	1.466	0.096	-0.125	14.195
0.676	1.428	0.049	-0.256	14.075	0.651	1.386	0.058	-0.277	13.781
0.322	1.206	0.278	-0.182	13.839	0.492	1.433	0.143	-0.264	13.802
0.185	1.222	0.471	-0.099	14.374	0.366	1.562	0.241	-0.212	13.873
0.122	1.341	0.603	-0.058	13.974	0.248	1.846	0.386	-0.142	13.636
0.080	1.451	0.736	-0.048	14.126	0.185	2.135	0.518	-0.125	13.863
0.055	1.522	0.822	-0.039	14.089	0.130	2.175	0.642	-0.095	13.877
0.037	1.563	0.883	-0.029	13.865	0.103	2.240	0.710	-0.081	13.715
0.019	1.611	0.950	-0.022	13.765	0.070	2.244	0.805	-0.062	13.615
0.011	1.621	0.987	-0.021	13.285	0.054	2.193	0.858	-0.054	13.523
-0.013	1.549	1.090	-0.009	13.874	0.026	1.975	0.963	-0.041	13.583
-0.011	1.555	1.088	-0.013	13.094	0.030	1.891	0.960	-0.047	13.181
0.003	1.530	1.059	-0.032	12.959	0.044	1.714	0.931	-0.068	13.258
0.016	1.485	1.030	-0.044	13.401	0.059	1.591	0.897	-0.081	13.590
0.046	1.506	0.949	-0.071	13.636	0.088	1.564	0.829	-0.107	13.831
0.058	1.490	0.926	-0.081	13.859	0.101	1.514	0.805	-0.119	14.039
0.079	1.529	0.888	-0.098	14.153	0.111	1.479	0.797	-0.126	14.305
0.056	1.502	0.982	-0.077	14.203	0.087	1.414	0.887	-0.102	14.335
0.033	1.577	1.137	-0.059	14.107	0.062	1.407	1.032	-0.086	14.239

As shown in Figure 1, the mass attenuation coefficients of the TW glasses can be ranked in the following order: TW20 > TW10 > TW0, indicating their relative capabilities to attenuate gamma radiation, with TW20 exhibiting the highest attenuation capacity and TW0 the lowest.

In radiation shielding design, the thickness of a material needed to reduce the incident photon intensity by 50% is a critical factor, as it directly impacts the material's ability to effectively absorb or attenuate radiation and ensure adequate radiation protection.

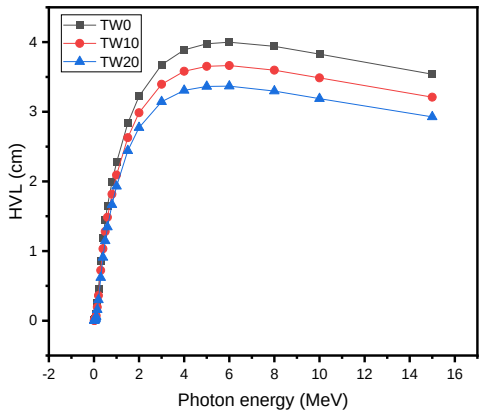

Figure 2(a). Half value layer as a function of photon energy.

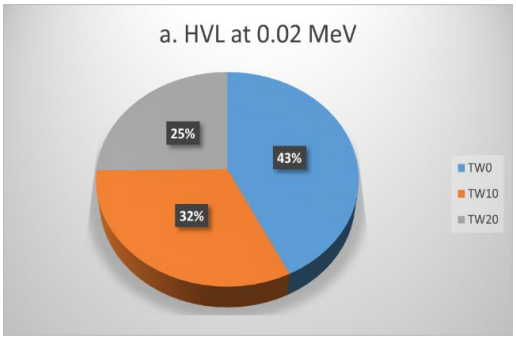

Figure 2(b). Half value layer as a function of WO_3 composition at 0.02 MeV photon energy.

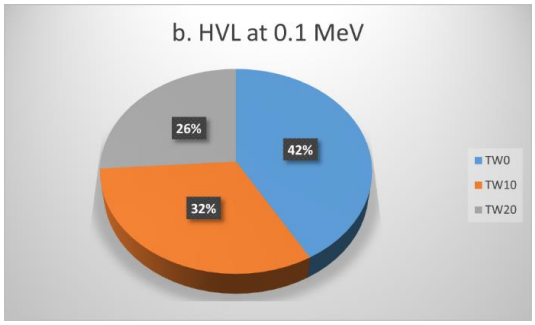

Figure 2(c). Half value layer as a function of WO_3 composition at 0.1 MeV photon energy

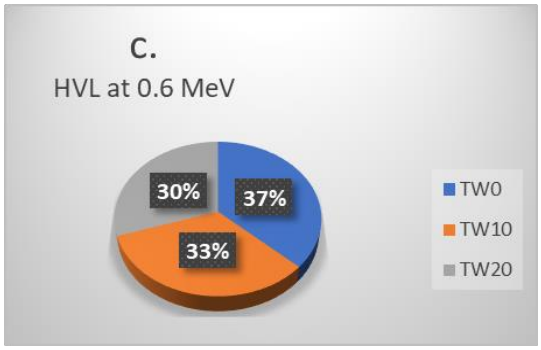

Figure 2(d). Half value layer as a function of WO_3 glass composition at 0.6 MeV photon energy.

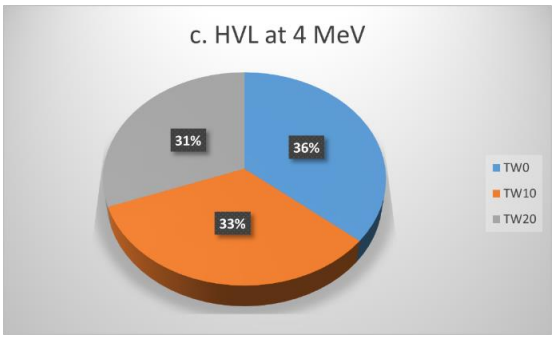

Figure 2(e). Half value layer as a function of WO_3 glass composition at 4 MeV photon energy.

Figure 2(a) displays the half-value layer (HVL) of the TW glasses as a function of photon energy, illustrating the energy-dependent shielding properties of the glasses. The impact of varying WO_3 concentrations on the HVL at distinct photon energies is further explored in Figures 2(b-e), which provide a detailed analysis of the effects of WO_3 content on radiation shielding performance across different energy ranges. The doping of WO_3 in the investigated glasses led to variations in their half-value layers (HVLs) at different photon energies. At 0.015 MeV, TW0 exhibited an HVL of 0.003 cm, whereas TW10 and TW20 showed lower HVLs of 0.002 cm each. Figure 2(a) The results show a consistent trend of decreasing HVL with rising WO_3 content. The notable effect of WO_3 doping on HVL is quantified in Figures 3(b-e), which display the percentage deviation in HVL at specific energies, highlighting the substantial influence of WO_3 on the photon shielding performance. Figure 2(b) shows that incorporating 10 mol% and 20 mol% WO_3 reduces the thickness of TW10 and TW20 samples by 6% and 16%, respectively, at 0.1 MeV. This decrease in half-value layer (HVL) is attributed to the increased density resulting from WO_3 addition, which rose by 10 %mol for TW10 and 20 %mol for TW20. Alternatively, these findings indicate that TW10 and TW20 exhibit enhanced absorption rates of 6% and 16%, respectively, at 0.1 MeV for the same thickness, due to the increased density. At intermediate photon energies, the photoelectric effect diminishes, and Compton scattering becomes the dominant interaction mechanism. In this region, the difference in properties between the samples is minimal, as shown in Figure 2(d), due to Compton scattering being primarily dependent on photon energy and only weakly dependent on atomic number (Z). However, at energies above 0.6 MeV, the half-value layer (HVL) of the samples decreases by 3% for TW10 and 7% for TW20 at 0.6 MeV, indicating a more significant effect of photon energy on HVL at higher energies.

Above the Compton scattering region, the difference in HVL of the samples was minimal due to multiple scattering events as the pair production process dominates the interaction above 4 MeV photon energy. TW10 and TW20 decreased by 2% and 7%, as 10 mol% and 20 mol% of WO_3 was incorporated.

Materials with a lower HVL are preferable for radiation shielding because they require less thickness to block radiation than materials with a higher thickness would. According to the significant difference in HVL between TW0, TW10, and TW20, TW20 with the highest WO_3 content possess smaller HVL at all photon energy as seen in Figure 2(a).

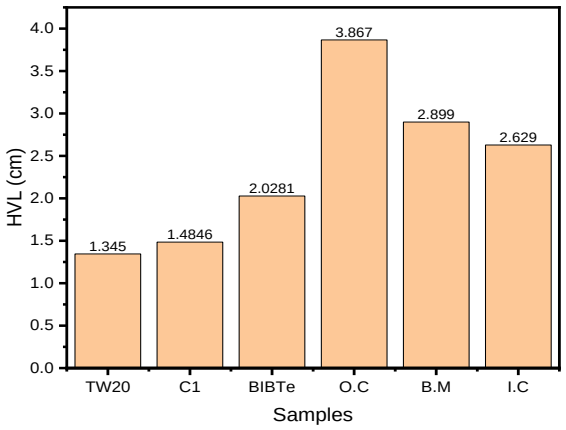

Figure 3. Comparison of HVL of TW20 glass with $60TeO_2+15B_2O_3+11Bi_2O_3+10Li_2O+1Ho_2O_3+3Yb_2O_3$ (C1) [40], 30BiBTe (BiBTe) [41], ordinary concrete (O.C) [42], Basalt-magnetite concrete (B.M) [42], Ilmenite concrete (I.C) [42].

Figure 3 presents a comparison of the half-value layer (HVL) of TW20 with other standard shielding materials. The results show that TW20 has a lower HVL compared to C1, BiBTe, O.C, B.M, and I.C, indicating its superior shielding capabilities. Therefore, TW20 emerges as the most effective shielding material among the compared materials, offering enhanced radiation attenuation properties.

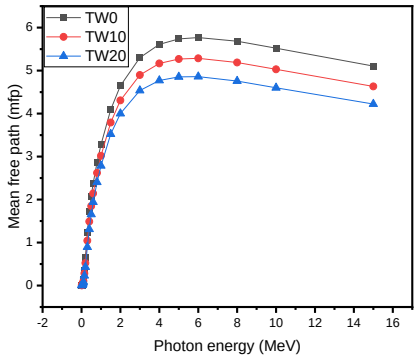

Figure 4. Mean free path as a function of the photon energy of the WT glasses.

The mean free path is the average distance traveled between collisions; a material of lower MFP provides better shielding ability. The MFP increased with increasing photon energy and decreased with an increasing WO_3 content as presented in Figure 4. The investigated glasses TW20, TW10, and TW0 provide MFP of 0.003, 0.04, 0.05 cm, and 4.222, 4.631, and 5.105 cm at 0.015 and 15 MeV photon energy. The differences in the MFP are associated with WO_3 content variation in the $(89-x)TeO_2+10TiO_2+1Nd_2O_3+xWO_3$ glass. According to the findings of the study, injecting 10 mol% and 20 mol% WO_3 caused the MFP to fall by 8.33% and 16.67%, respectively (see Figure 4). The TW20 provides the lowest MFP irrespective of photon energies among the other samples and, therefore, provides the best shielding characteristics in agreement with other shielding parameters.

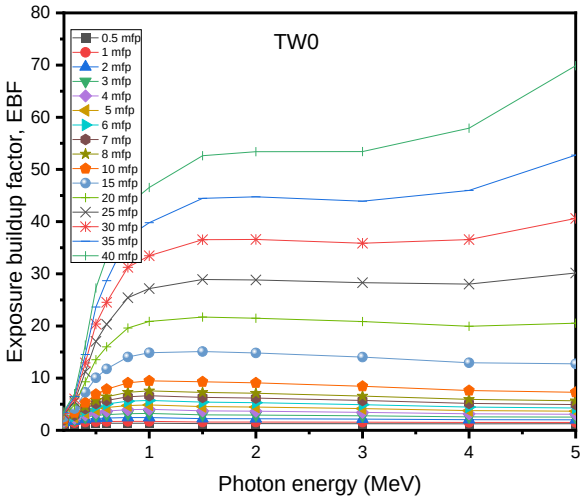

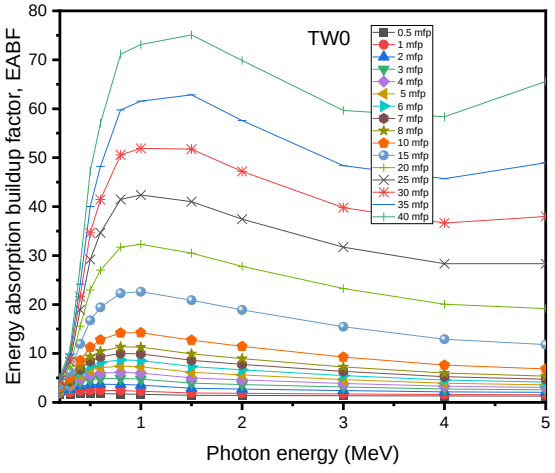

Figure 5. Exposure buildup factor and energy absorption buildup factor for WT0 glass sample

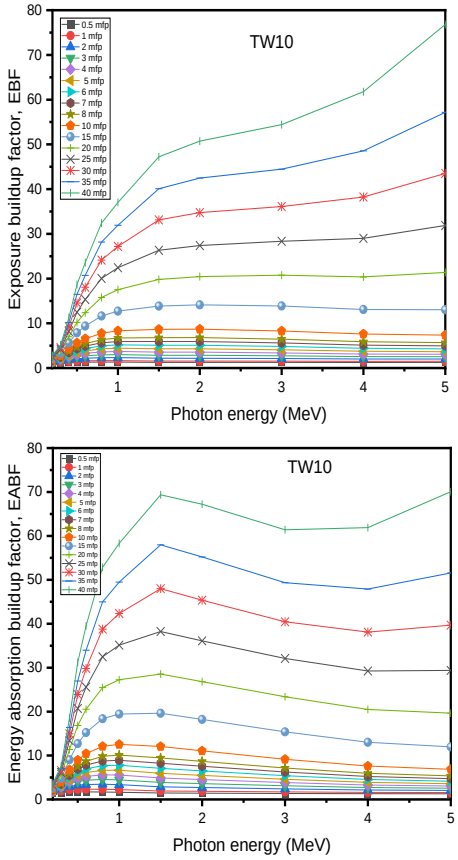

Figure 6. Exposure buildup factor and energy absorption buildup factor for WT10 glass sample

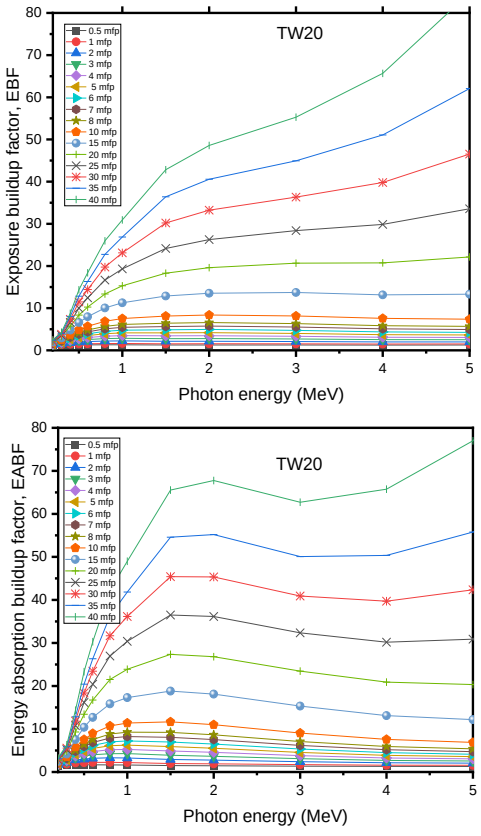

Figure 7. Exposure buildup factor and energy absorption buildup factor for WT20 glass sample

The exposure buildup factor and energy absorption buildup factor are important components in radiation shielding examinations. The G-P fitting shown in Table 3, Table 4, and Table 5 was used to estimate the EBF and EABF for the investigated TW0, TW10, and TW20 glasses.

Figures 7, 8, and 9 show the plot of EBF and EABF of the examined TW glasses as a function of photon energy from 0.15 MeV to 15 MeV and penetration depth of 0.5 to 40 mfp.

Because of photoelectric absorption, the change in buildup factor as a function of photon energy was minimal for all samples of TW glasses in the lower energy range and it increases with increasing penetration depth. WT20 with 20 mol% WO_3 concentrations has the lowest EBF and EABF due to WO_3 contribution to photon absorption compared with TW0 and TW10 samples. At intermediate photon energy where Compton scattering dominates the interaction process, the buildup factors increase to a maximum with increasing penetration depth. possibly due to secondary photons generated through repeated collisions. At this region, EBF and EABF decrease with increasing WO_3 content and WT glass has the minimum buildup factors as shown in Figure 5, Figure 6, and Figure 7, respectively. EBF and EABF increase beyond the Compton scattering energy range and increase with increasing penetration depth, as pair formation dominates the interaction process.

Furthermore, TW glass's ability to block neutron particles was investigated. The effective removal cross-section $\sum_R(cm^2.g^{-1})$ was calculated using the equation proposed by Abd et al . [43] for fast neutrons effective removal cross-section from the following equations;

$$\sum_R(cm^2.g^{-1}) = 0.190Z^{-0.743}\ (Z \leq 8) \qquad (12)$$

$$\sum_R(cm^2.g^{-1}) = 0.125Z^{-0.565}\ (Z > 8) \qquad (13)$$

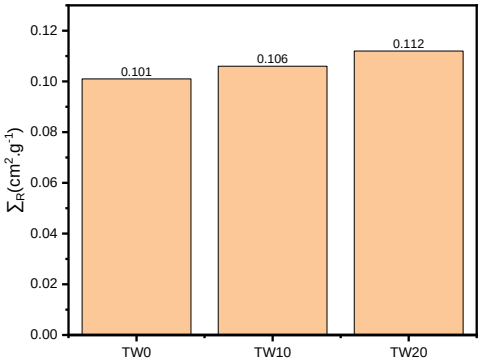

Figure 8. Fast neutron effective removal cross-section of the investigated WT glasses.

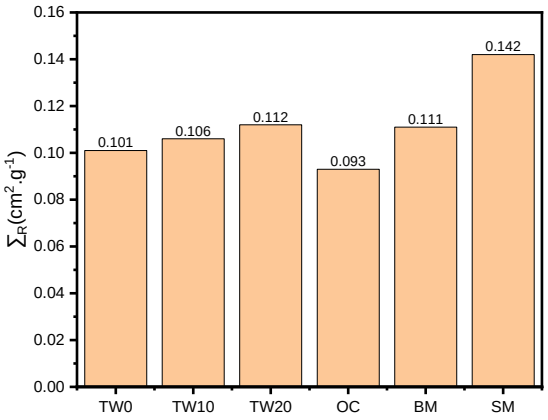

Figure 9. Comparison of the effective fast neutron removal cross sections of TW glasses, ordinary concrete (OC), Basalt (BM), and steel magnetite.

As shown in Figure 8, the effective cross sections for fast neutron removal for TW0, TW10, and TW20 are 0.101, 0.106, and 0.112 cm^{-1}, respectively. In the absence of WO_3 in TW glass, the effective neutron removal cross-section was 0.101 cm^{-1} and increased as the WO_3 level increases from 10 mol% to 20 mol% corresponding to 0.106 and 0.112 cm^{-1}, respectively. The addition of 10 mol% and 20 mol% WO_3 increased the effective removal of fast neutron cross section by 1.57 % and 1.88 % for TW10 and TW20, respectively. WT20 has a higher effective fast neutron removal cross-section compared to some standard shielding materials. As shown in Figure 9, TW20 has an effective fast neutron removal cross-section higher than that of ordinary concrete and basalt, but lower than that of steel magnetite. Therefore, the TW20 glasses investigated could potentially be used as a protective shield against gamma rays and fast neutron particles.

4. Conclusion

This study examines the radiation-shielding capabilities of tungsten-doped titanium neodymium tellurite glasses of composition (89-x)TeO_2–10TiO_2– 1Nd_2O_3–xWO_3, x = 0, 10 and 20 mol%. the glasses coded TW0, TW10, and TW20 have been investigated for gamma and neutron shielding ability using Phy-X and XCOM program. The mass attenuation coefficient increased with increasing WO_3 concentration and decreased with increasing photon energy. Sample with larger WO_3 (20 mol%) has the highest MAC, and MFP values at all photon energies. The EBF and energy absorption buildup factor EABF decreases as the concentration of WO_3 increases, but increases with greater penetration depth. Notably, WT glasses outperform certain common materials in terms of their ability to shield against gamma rays and effectively absorb fast neutrons. This highlights the significant potential of utilizing existing glass as effective shield against both gamma and neutron radiation.

Conflict of interest

The authors declare no conflict of interest.

Acknowledgements

The authors wish to express their sincere appreciation to the Tertiary Education Trust Fund (TETFund) Nigeria (TETF/ES/UNIV/SOKOTO/TSAS/2020) for their generous support of my Ph.D. program. Additionally, they extend their gratitude to University Technology Malaysia, particularly the staff of the Physics department, for providing a supportive and enriching environment, as well as expert guidance, which contributed significantly to the success of this research.

References

1. Kharita, M., S. Yousef, and M. AlNassar, *The effect of the initial water to cement ratio on shielding properties of ordinary concrete.* Prog. Nucl. Energy, 2010. **52**(5): p. 491-493.
2. Akkurt, I., C. Basyigit, S. Kilincarslan, B. Mavi, and A. Akkurt, *Radiation shielding of concretes containing different aggregates.* Cement and Concrete Composites, 2006. **28**(2): p. 153-157.
3. Mesbahi, A. and H. Ghiasi, *Shielding properties of the ordinary concrete loaded with micro-and nano-particles against neutron and gamma radiations.* Appl. Radiat. Isot., 2018. **136**: p. 27-31.
4. Tekin, H.O., V.P. Singh, and T. Manici, *Effects of micro-sized and nano-sized WO3 on mass attenauation coefficients of concrete by using MCNPX code.* Appl. Radiat. Isot., 2017. **121**: p. 122-125.
5. Abdel Wahab, E., K.S. Shaaban, R. Elsaman, and E.S. Yousef, *Radiation shielding and physical properties of lead borate glass-doped ZrO 2 nanoparticles.* Appl. Phys. A, 2019. **125**: p. 1-15.
6. Nagaraj, N., H. Manjunatha, Y. Vidya, L. Seenappa, K. Sridhar, and P.D. Gupta, *Investigations on Lanthanide polymers for radiation shielding purpose.* Radiat. Phys. Chem., 2022. **199**: p. 110310.
7. Zughbi, A., M. Kharita, and A. Shehada, *Determining optical and radiation characteristics of cathode ray tubes' glass to be reused as radiation shielding glass.* Radiat. Phys. Chem., 2017. **136**: p. 71-74.
8. Xie, J., J. Zhang, Z. You, S. Liu, K. Guan, R. Wu, J. Wang, and J. Feng, *Towards developing Mg alloys with simultaneously improved strength and*

corrosion resistance via RE alloying. Journal of Magnesium and Alloys, 2021. **9**(1): p. 41-56.
9. Yin, S., W. Duan, W. Liu, L. Wu, J. Bao, J. Yu, L. Li, Z. Zhao, J. Cui, and Z. Zhang, *Improving the corrosion resistance of MgZn1. 2GdxZr0. 18 (x= 0, 0.8, 1.4, 2.0) alloys via Gd additions.* Corrosion Science, 2020. **177**: p. 108962.
10. Al-Hadeethi, Y. and M. Sayyed, *Analysis of borosilicate glasses doped with heavy metal oxides for gamma radiation shielding application using Geant4 simulation code.* Ceram. Int., 2019. **45**(18): p. 24858-24864.
11. Sayyed, M., K.M. Kaky, D. Gaikwad, O. Agar, U. Gawai, and S. Baki, *Physical, structural, optical and gamma radiation shielding properties of borate glasses containing heavy metals (Bi2O3/MoO3).* J. Non·Cryst. Solids, 2019. **507**: p. 30-37.
12. Lacomme, E., M. Sayyed, H. Sidek, K. Matori, and M. Zaid, *Effect of bismuth and lithium substitution on radiation shielding properties of zinc borate glass system using Phy-X/PSD simulation.* Results Phys., 2021. **20**: p. 103768.
13. Rammah, Y., A. Ali, R. El-Mallawany, and F. El-Agawany, *Fabrication, physical, optical characteristics and gamma-ray competence of novel bismo-borate glasses doped with Yb2O3 rare earth.* Physica B Condens. Matter, 2020. **583**: p. 412055.
14. Kaky, K.M., G. Lakshminarayana, S. Baki, I. Kityk, Y. Taufiq-Yap, and M. Mahdi, *Structural, thermal and optical absorption features of heavy metal oxides doped tellurite rich glasses.* Results Phys., 2017. **7**: p. 166-174.
15. Divina, R., G. Sathiyapriya, K. Marimuthu, A. Askin, and M. Sayyed, *Structural, elastic, optical and γ-ray shielding behavior of Dy3+ ions doped heavy metal incorporated borate glasses.* J. Non·Cryst. Solids, 2020. **545**: p. 120269.
16. Saddeek, Y.B., K.A. Aly, K.S. Shaaban, A.M. Ali, and M.A. Sayed, *The effect of TiO 2 on the optical and mechanical properties of heavy metal oxide borosilicate glasses.* Silicon, 2019. **11**: p. 1253-1260.
17. Adewinbi, S., W. Buremoh, V. Owoeye, Y. Ajayeoba, A. Salau, H. Busari, M. Tijani, and B. Taleatu, *Preparation and characterization of TiO2 thin film electrode for optoelectronic and energy storage potentials: effects of Co incorporation.* Chem. Phys. Lett., 2021. **779**: p. 138854.
18. Al-Buriahi, M., Z. Alrowaili, C. Eke, J.S. Alzahrani, I. Olarinoye, and C. Sriwunkum, *Optical and radiation shielding studies on tellurite glass system containing ZnO and Na2O.* Optik, 2022. **257**: p. 168821.
19. Hanfi, M., M. Sayyed, E. Lacomme, I. Akkurt, and K. Mahmoud, *The influence of MgO on the radiation protection and mechanical properties of tellurite glasses.* Nucl. Eng. Technol., 2021. **53**(6): p. 2000-2010.
20. Uosif, M., A. Mostafa, Z. Alrowaili, R. Elsaman, A. Showahy, S.A. Issa, and Y.B. Saddeek, *Effects of Nd2O3 substitution on the mechanical and radiation shielding properties of alumino-borobismuthate glasses.* Eur. Phys. J. Plus . 2021. **136**(4): p. 427.
21. Boodaghi Malidarre, R. and I. Akkurt, *The influence of Nd2O3 on the radiation shielding, physical, mechanical, and acoustic properties of the (75− x) TeO2–15 MgO–10 Na2O–x Nd2O3 glasses as a potent radiation shielding material.* Polymer Composites, 2022. **43**(8): p. 5418-5425.
22. Mahmoud, I., M. Gaafar, S. Marzouk, A. Okasha, and H. Saudi, *The characteristics of Nd2O3 in ZnO lead phosphate glasses regarding their mechanical, structural, and shielding properties.* Appl. Phys. A, 2022. **128**(10): p. 938.
23. Kilic, G., *Role of Nd 3+ ions in TeO 2–V 2 O 5–(B 2 O 3/Nd 2 O 3) glasses: Structural, optical, and thermal characterization.* J. Mater. Sci. Mater, 2020. **31**: p. 12892-12902.
24. Gedam, R. and D. Ramteke, *Electrical and optical properties of lithium borate glasses doped with Nd2O3.* J. of Rare Earths, 2012. **30**(8): p. 785-789.
25. Iliyasu, U., M.S.M. Sanusi, and N.E. Ahmad, *The effect of WO3 on the optical and radiation shielding properties of zinc-lead-borate glass.* Radiat. Phys. Chem., 2023: p. 111007.
26. Al-Buriahi, M., T. Taha, M.A. Alothman, H. Donya, and I. Olarinoye, *Influence of WO3 incorporation on synthesis, optical, elastic and radiation shielding properties of borosilicate glass system.* Eur. Phys. J. Plus . 2021. **136**(7): p. 779.
27. Alzahrani, J.S., A. Sharma, S. Nazrin, Z. Alrowaili, and M. Al-Buriahi, *Optical and radiation shielding effectiveness of a newly fabricated WO3 doped TeO2–*

B2O3 glass system. Radiat. Phys. Chem., 2022. **193**: p. 109968.
28. Aloraini, D.A., A.H. Almuqrin, M. Sayyed, A. Kumar, D. Gaikwad, D.I. Tishkevich, and A. Trukhanov, *Experimental and theoretical analysis of radiation shielding properties of strontium-borate-tellurite glasses.* Opt. Mater., 2021. **121**: p. 111589.
29. Abouhaswa, A., M. Sayyed, A.S. Altowyan, Y. Al-Hadeethi, and K. Mahmoud, *Synthesis, structural, optical and radiation shielding features of tungsten trioxides doped borate glasses using Monte Carlo simulation and phy-X program.* J. Non·Cryst. Solids, 2020. **543**: p. 120134.
30. Mhareb, M., Y. Alajerami, N. Dwaikat, M. Al-Buriahi, M. Alqahtani, F. Alshahri, N. Saleh, N. Alonizan, M. Saleh, and M. Sayyed, *Investigation of photon, neutron and proton shielding features of H3BO3–ZnO–Na2O–BaO glass system.* Nucl. Eng. Technol., 2021. **53**(3): p. 949-959.
31. Kebaili, I., I. Boukhris, and M. Sayyed, *Gamma-ray shielding properties of lead borovanadate glasses.* Ceram. Int., 2020. **46**(11): p. 19624-19628.
32. Şakar, E., Ö.F. Özpolat, B. Alım, M. Sayyed, and M. Kurudirek, *Phy-X/PSD: development of a user friendly online software for calculation of parameters relevant to radiation shielding and dosimetry.* Radiat. Phys. Chem., 2020. **166**: p. 108496.
33. Berger, M.J., *XCOM: photon cross sections database.* http://physics. nist. gov/PhysRefData/Xcom/Text/XCOM. html, 1998. **8**: p. 3587.
34. Tekin, H., E. Kavaz, A. Papachristodoulou, M. Kamislioglu, O. Agar, E.A. Guclu, O. Kilicoglu, and M. Sayyed, *Characterization of SiO2–PbO–CdO–Ga2O3 glasses for comprehensive nuclear shielding performance: Alpha, proton, gamma, neutron radiation.* Ceram. Int., 2019. **45**(15): p. 19206-19222.
35. Kumar, A., D. Gaikwad, S.S. Obaid, H. Tekin, O. Agar, and M. Sayyed, *Experimental studies and Monte Carlo simulations on gamma ray shielding competence of (30+ x) PbO10WO3 10Na2O− 10MgO–(40-x) B2O3 glasses.* Prog. Nucl. Energy, 2020. **119**: p. 103047.
36. Rammah, Y., I. Olarinoye, F. El-Agawany, and A. El-Adawy, *The f-factor, neutron, gamma radiation and proton shielding competences of glasses with Pb or Pb/Bi heavy elements for nuclear protection applications.* Ceram. Int., 2020. **46**(17): p. 27163-27174.
37. Agar, O., M. Sayyed, F. Akman, H. Tekin, and M. Kaçal, *An extensive investigation on gamma ray shielding features of Pd/Ag-based alloys.* Nucl. Eng. Technol., 2019. **51**(3): p. 853-859.
38. Sayyed, M., *Half value layer, mean free path and exposure buildup factor for tellurite glasses with different oxide compositions.* J. Alloys Compd., 2017. **695**: p. 3191-3197.
39. Sayyed, M., S.A. Issa, and S.H. Auda, *Assessment of radio-protective properties of some anti-inflammatory drugs.* Prog. Nucl. Energy, 2017. **100**: p. 297-308.
40. Naaim, M., M. Malek, M. Sayyed, N. Sahapini, and R. Hisam, *Impact of TeO2–B2O3 manipulation on physical, structural, optical and radiation shielding properties of Ho/Yb codoped mixed glass former borotellurite glass.* Ceram. Int., 2023. **49**(7): p. 10342-10353.
41. Halimah, M., A. Azuraida, M. Ishak, and L. Hasnimulyati, *Influence of bismuth oxide on gamma radiation shielding properties of boro-tellurite glass.* J. Non·Cryst. Solids, 2019. **512**: p. 140-147.
42. Kumar, A., *Gamma ray shielding properties of PbO-Li2O-B2O3 glasses.* Radiat. Phys. Chem., 2017. **136**: p. 50-53.
43. El Abd, A., G. Mesbah, N.M. Mohammed, and A. Ellithi, *A simple method for determining the effective removal cross section for fast neutrons.* J. Radiat. Nucl. Appl, 2017. **2**(2): p. 53-58.

